Journal of Thermal Analysis and Calorimetry (2024) 149:10017–10029
https://doi.org/10.1007/s10973-024-13358-3

Numerical exploration of the entropy generation in tri-hybrid nanofluid flow across a curved stretching surface subject to exponential heat source/sink

Asif Ullah Hayat[1] · Hassan Khan[1] · Ikram Ullah[2] · Hijaz Ahmad[3,4,5,6] · Mohammad Mahtab Alam[7] · Muhammad Bilal[8]

Received: 19 April 2024 / Accepted: 28 May 2024 / Published online: 30 July 2024

Abstract

Ternary hybrid nanofluids (Thnf) are used in several fields, including enhancements of heat transfer, solar power systems, medical devices, electronics cooling, aviation industry, and automotive sector. Furthermore, Thnf provide a versatile solution to boost energy transport for the industrial applications. In the current analysis, an incompressible magnetized Thnf flow with the natural convection through a curved surface using Darcy–Forchheimer medium is addressed. The heat transfer is simulated by using the Cattaneo–Christov (C–C) heat flux model. Aluminum alloys (Ti_6Al_4V, AA7072 and AA7075) are dispersed in water (H_2O) and ethylene glycol ($C_2H_6O_2$) to synthesize the modified hybrid nanofluid. The model equations are reform into ODEs (ordinary differential equations) by using the similarity substitution. The non-dimensional set of ODEs is further numerically estimated through PCM (Parametric continuation method). The physical behavior of velocity, energy outline, Nusselt number and skin friction for distinct values of emerging variables are computed and analyzed in detail. The finding reveals that an improvement in entropy generation has been observed versus the rising values of unsteadiness and variable porosity parameters. The rising effect of permeability parameter enhances the velocity curve; whereas, fluid velocity drops with the influence of inertia coefficient.

Keywords Entropy generation · Cattaneo–Christov heat flux · Aluminum alloys · Thermal radiation · Variable Darcy–Forchheimer law · Curved surface

✉ Hijaz Ahmad
hijazahmad@duytan.edu.vn; hijaz.ahmad@neu.edu.tr

[1] Department of Mathematics, Abdul Wali Khan University, Mardan 23200, Pakistan

[2] Department of Natural Sciences and Humanities, University of Engineering and Technology, Mardan 23200, Pakistan

[3] Institute of Research and Development, Duy Tan University, Da Nang, Vietnam

[4] School of Engineering and Technology, Duy Tan University, Da Nang, Vietnam

[5] Operational Research Center in Healthcare, Near East University, TRNC Mersin 10, 99138 Nicosia, Turkey

[6] Department of Mathematics, Faculty of Science, Islamic University of Madinah, Madinah, Saudi Arabia

[7] Department of Basic Medical Sciences, College of Applied Medical Science, King Khalid University, 61421 Abha, Saudi Arabia

[8] Sheikh Taimur Academic Block-II, Department of Mathematics, University of Peshawar, Peshawar 25120, Khyber Pakhtunkhwa, Pakistan

List of symbols

K	Curvature parameter
P	Pressure (Kg m^{-1} s^{-2})
η	Similarity variable
T_∞	Ambient temperature (K)
F'	Dimensionless velocity
μ	Dynamic viscosity (Kg m^{-1}s^{-1})
Br	Brinkman number
α	Permeability parameter
ν	Kinematic viscosity (m^{-1} s^{-2})
Ra	Radiation variable
q_{w}	Heat flux
Q	Temperature-dependent heat source
γ	Length dimension
T_{w}	Wall temperature (K)
ε	Porosity of the porous medium
d_1	Variable permeability
k_{r}	Chemical reaction rate (mol L^{-1} s^{-1})
ε_∞	Surface porosity
Qe	Exponential heat source

k	Thermal conductivity (W m^{-1} K^{-1})
C_b	Drag coefficient
Ec	Eckert number
γ_1	Temperature ratio parameter
Re_s	Reynold number
α^*	Thermal diffusivity
F	Stream function
u, v	Velocity components
B_0	Magnetic field strength
C_p	Specific heat capacity (J Kg K^{-1})
$b<0$	Shrinking sheet
M	Dimensionless magnetic field
θ	Dimensionless temperature
ρ	Density (Kg m^{-3})
Pr	Prandtl number
T	Temperature of fluid (K)
S	Dimensionless heat source parameter
σ^*	Stefan–Boltzmann constant
d_2	Variable porosity
β_1	Thermal relaxation parameter
$\hat{k}$	Porosity term
C	Unsteadiness parameter
$k*$	Coefficient of mean absorption (m^{-1})
k_1	Boltzmann constant (8.314 J mol^{-1} K^{-1})
$b=0$	Static sheet
k_∞	Surface permeability
u_w	Stretching velocity
β	Inertia coefficient
$b>0$	Stretching sheet
τ_{rs}	Shear stress
λ_E	Relaxation time heat flux

Subscripts

Thnf	Ternary hybrid nanofluid
hnf	Hybrid nanofluid
f	Fluid
nf	Nanofluid
bf	Base fluid

Introduction

The researchers are taking interested in energy transfer with fluid flow across a curved surface due to its practical significance in various manufacturing sectors including the aerodynamics of vehicles, extraction of polymeric sheets, turbine blades, glass fiber, ship design, heat exchangers, hot rolling, paper production, wind turbines sports equipment, and biomedical applications. Ullah et al. [1] examined thermal transfer in hybrid nanofluid Darcy–Forchheimer flows subjected to various shape impact across a curved stretching surface (CSS). Incorporating carbon nanotubes and iron ferrite nanoparticles (NPs), Gohar et al. [2] investigated the movement of Casson Hnf (hybrid nanofluid) across a CSS. The flow of Hnf across a porous exponential CSS with thermal slip and suction/ injunction effect was assessed by Abbas et al. [3]. According to the outcomes, the positive coefficient of curvature factor increased the velocity field for both the injection and suction scenarios. Raza et al. [4] examined the thermal transportation characteristics of a radiative Hnf flow over a CSS. The findings revealed that the curvature factor has a moderating effect on the velocity field. Ahmed et al. [5] described the dynamics of magnetohydrodynamic (MHD) steady 2D flow of Hnf across a CSS with the homogeneous–heterogeneous reactions. Xiong et al. [6] investigated the magnetized Darcy laminar flow of viscous fluid over a CSS with the effects of second-order slip. Ali and Jubair [7] explored the rheological features of Hnf flow with heat source and thermal emission across a CSS. The outcome demonstrates that the velocity field is raised but the energy is decreased for greater curvature coefficient. Hayat et al. [8] reported the flow of radiative hybrid nanomaterials via a porous curving surface with Joule heating and inertial features. The results indicated that the velocity curve is enhances when the curvature factor rises; while, the opposite tendency is found concerning the magnetic parameters. Using a stretchable curved oscillatory surface, Imran et al. [9] considered the impact of Soret and Dufour on the MHD flow of unsteady couple stress fluid. Employing joule heating and viscous dissipation effect, Haq and Ashraf [10] evaluated the entropy generation of MHD convective flow of Carreau fluid on a CSS. Recently several authors have reported on curved stretching surface [11–14].

As the world's population continues to expand at a rapid rate, there will be an ever-increasing demand for energy consumption that is more efficient. Efficient and rapid heat transfer inside a thermal system necessitates the use of high-performance thermal management systems due to the elevated temperatures concerned. Nanofluids have garnered significant interest in recent times, especially regarding their use in renewable energy systems and techniques to enhance heat transfer. Nanofluids are considered to comprise particles with diameters of nanometers suspended in base fluids, such as water or motor oil, creating a completely new class of fluids called nanofluids. Metal or carbon are the most common materials for nanoparticles utilized in nanofluids. There are numerous applications for nanofluid as a coolant in the engineering, automotive industry, nuclear coolant, renewable energy and healthcare sectors. The term "nanofluid" (NF) was 1st used by Choi and Eastman [15] in 1995 and Buongiorno [16] demonstrated that NF are formed by combining nanoparticles with base fluids. The effects of MHD convective free stream NF flow across a stretching cylinder were studied by Makkar et al. [17]. Hnf and Thnf exhibit enhanced thermal properties when compared to standard NF. A base fluid is used to synthesize Thnfs and

Hnfs, respectively, by incorporating two or more distinct NPs into the base fluid. The numerical analysis emphasizes the flow of a nano-liquid containing hybrid nanoparticles (AA7072, AA7075) via an endless disc was performed by Ullah et al. [18]. With the use of aluminum alloys, Hanif et al. [19] examined the two-dimensional water-based Hnf flow through an inclined sheet with suction and Joule heating effect. A 3-D Hnf flow of methanol and AA7072–AA7075 with slip effect was studied by Tlili et al. [20] on an irregular surface. Archana et al. [21] considered the effect of radiative heat transfer on the mobility of ternary alloys consisting of Nimonic 80A and aluminum alloys (AA7072–AA7075) over a melting surface. Manjunatha et al. [22] investigated the Thnf flow across a two-dimensional enlarging surface. Recently significant results are presented by Ref. [23–29].

Understanding a system's irreversibility factor in heat transfer processes requires an understanding of entropy generation, especially in conventional industrial sectors where fluid fluxes and heat transmission are involved. The formation of entropy is a significant feature of thermodynamics. In a thermal system that is isolated from other systems, the second law of thermodynamics asserts that entropy does not diminish. Total entropy is continually increasing in irreversible phenonium; whereas, it is always remaining identical in reversible processes. The entropy formation is the idea that plays an essential role in comprehending and increasing the efficiency of a wide variety of systems and procedures including air conditioning, heat transfer devices, air conditioning units, combustion, vehicle engines, reactors, chillers, and desert coolers [30]. Khan and Alzahrani [31] and Naveed [32] used the Joule heating, thermophoresis and Brownian motion effect for Blasius flow on a curving surface to analyze the entropy formation of a chemically reactive nanofluid. Ibrahim and Gizewu [33] investigated the bioconvective formation of entropy and gyrotactic microbes incompressible, viscous flow over a curving extended surface. The entropy formation in MHD Hnf flow with variable porosity was investigated by Hayat et al. [34]. Employing Arrhenius activation energy and entropy optimization, Alsallami et al. [35] simulated the Marangoni Maxwell nanofluid flowing on a spinning disc. Murtaza et al. [36] addressed the numerical simulation for entropy formation and thermal transport through tri-hybrid nanoliquid. Sakkaravarthi and Reddy [37] employed blood as the base fluid to assess the formation of entropy in MHD Hnf flow comprised of silver and aluminum oxide NPs across a porous surface with Joule heating and convective boundary circumstances. The references [38–41] provide some of the additional investigations that are associated with the entropy formation of a fluid flow over a curving extended surface.

Based on the above literature, no one has described the C–C heat flux model using Thnf flow with viscous dissipation across a porous curved surface. In order to fill such gap, the current research work focuses on the Thnf flow encompassed of aluminum alloys (Ti_6Al_4V, AA7072 and AA7075) across curved stretching surface. The flow has been numerically assessed under the consequences of heat radiation, Joule heating and C–C theory, viscous dissipation, and exponential heat source. Some core novelties are:

- To investigate the heat transfer subject to C–C heat flux, viscous dissipation, thermal radiation and EHS.
- To study the Thnf flow across a permeable curved surface.
- To examine the consequences of Ti_6Al_4V, AA7072 and AA7075-NPs on the fluid velocity and heat transfer rate.
- What is the impact of thermal time relaxation factor on temperature?
- What is the effect of Darcy medium with varying porosity and permeability has on the flow of the Thnf?

Mathematical modeling

The 2D incompressible Thnf flow across a porous CSS of radius R is considered. Variations on the Darcy–Forchheimer relation are employed to characterize the flow in permeable surface. The addition of C–C heat flux, radiation and Joule heating to the energy expression contributes to the enhancement of the thermal field. The velocity of stretching surface along the s-axis is denoted by $u_w = \frac{\mathrm{bs}}{(1-\alpha^* t)}$ where $b > 0$ (see Fig. 1). Here $b = 0$ correspond to static sheet and $b > 0$ describes the stretching of curved surface. In r-direction, a magnetic field with intensity $\overrightarrow{B_0}$ is integrated. The surface's temperature is described as T_w. Entropy generation is also computed using the 2nd law of thermodynamics. The following equations are based on the above assumptions [34, 42]:

$$\frac{\partial \rho}{\partial t} + \vec{\nabla} \cdot (\rho \vec{V}) = 0, \tag{1}$$

For incompressible fluid ρ is constant so $\frac{\partial \rho}{\partial t} = 0$, Eq. (1) become

$$\vec{\nabla} \cdot \vec{V} = 0, \tag{2}$$

In a curvilinear coordinate the continuity equation become,

$$\left(-R\frac{\partial u}{\partial s}\right) = \frac{\partial((r+R)v)}{\partial r}, \tag{3}$$

$$\frac{\partial p}{\partial r} = \rho_{\mathrm{Thnf}}\left(\frac{u^2}{r+R}\right), \tag{4}$$

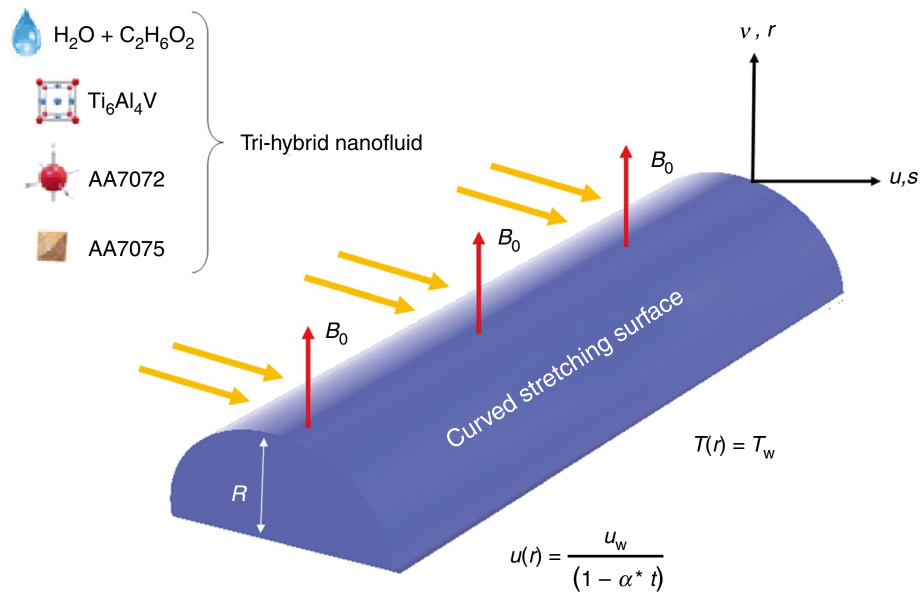

Fig. 1 Physical visualization of the flow

$$\frac{\partial u}{\partial t}+v\left(\frac{\partial u}{\partial r}\right)+\left(\frac{u}{r+R}\right)\left(R\left(\frac{\partial u}{\partial s}\right)+v\right)$$
$$=\frac{-R}{\rho_{\text{Thnf}}(R+r)}\left(\frac{\partial P}{\partial s}\right)-\frac{C_b\varepsilon^2(r)}{(k^*(r))^{\frac{1}{2}}}u^2$$
$$+\nu_{\text{Thnf}}\left(\frac{\partial^2 u}{\partial r^2}+u\frac{1}{(R+r)}\left(\frac{\partial u}{\partial r}-\frac{u}{(R+r)}\right)-\frac{\varepsilon(r)}{k^*(r)}\right)-\frac{\sigma_{\text{Thnf}}}{\rho_{\text{Thnf}}}B_0^2u, \tag{5}$$

$$\frac{\partial T}{\partial t}+u\left(\frac{R}{R+r}\right)\frac{\partial T}{\partial s}+\lambda_E\Phi_E+v\left(\frac{\partial T}{\partial r}\right)$$
$$=\frac{k_{\text{Thnf}}}{(\rho C_p)_{\text{Thnf}}}\left(\frac{\partial^2 T}{\partial r^2}-\frac{1}{(R+r)}\frac{\partial T}{\partial r}\right)$$
$$+\frac{16\sigma^* T_\infty^3}{3k^*(\rho C_p)_{\text{Thnf}}}\left(\frac{\partial^2 T}{\partial r^2}-\frac{1}{(R+r)}\frac{\partial T}{\partial r}\right)$$
$$+\frac{Q}{(\rho C_p)_{\text{Thnf}}}(T-T_\infty)e^{-r\sqrt{\left(\frac{u_w}{\nu_f}\right)}}$$
$$+\frac{\sigma_{\text{Thnf}}B_0^2u^2}{(\rho C_p)_{\text{Thnf}}}+\frac{\mu_{\text{Thnf}}}{(\rho C_p)_{\text{Thnf}}}\frac{\varepsilon(r)}{k^*(r)}u^2+\frac{\rho_{\text{Thnf}}}{(\rho C_p)_{\text{Thnf}}}\frac{C_b\varepsilon^2(r)}{(k^*(r))^{\frac{1}{2}}}u^3, \tag{6}$$

where

$$\Phi_E=\frac{\partial^2 T}{\partial t^2}+\frac{\partial v}{\partial t}\frac{\partial T}{\partial r}+2v\frac{\partial}{\partial r}\left(\frac{\partial T}{\partial t}\right)$$
$$+\left(\frac{R}{R+r}\right)\left(2u\frac{\partial}{\partial s}\left(\frac{\partial T}{\partial t}\right)+\frac{\partial T}{\partial s}\frac{\partial u}{\partial t}+u^2\left(\frac{R}{r+R}\right)\left(\frac{\partial^2 T}{\partial s^2}\right)\right)$$
$$+v^2\frac{\partial^2 T}{\partial r^2}+\left(\frac{uR}{r+R}\left(2v\left(\frac{\partial T}{\partial s}\right)+\frac{\partial v}{\partial s}\right)+v\left(\frac{\partial v}{\partial r}\right)\right)\frac{\partial T}{\partial r}$$
$$+\left(v\frac{\partial u}{\partial r}+u\left(\frac{\partial u}{\partial s}-v\right)\left(\frac{R}{R+r}\right)\right)\left(\frac{R}{R+r}\right)\frac{\partial T}{\partial s}, \tag{7}$$

$$\varepsilon(r)=\left(1+d_2e^{-\left(\frac{r}{\gamma}\right)}\right)\varepsilon_\infty,\quad \frac{k^*(r)}{k_\infty}=\left(1+d_1e^{-\left(\frac{r}{\gamma}\right)}\right). \tag{8}$$

In the above equations, $(\rho C_p)_{\text{Thnf}}$ is the volumetric heat capacity, k^* demonstrates the porosity term, (u, v) are the component of the velocity, γ is the constant length of dimension, ε_∞ is the surface porosity, λ_E is the time relaxation heat flux, k_∞ is the surface permeability, B_0 is the magnetic field strength, α^* is the thermal diffusivity, C_b is the drag coefficient, d_1 is the variable permeability k_{Thnf} demonstrates the thermal conductivity, d_2 is the variable porosity, ρ_{Thnf} is the density, σ_{Thnf} is the electrical conductivity, σ^* is the Stefan Boltzmann coefficient and ν_{Thnf} is the kinematic viscosity as show in Table 1.

The appropriate boundary conditions (BCs) are:

$$\left.\begin{array}{l} u(r)=\frac{u_w}{(1-\alpha^* t)},\quad T(r)=T_w,\quad v(r)=0,\ \text{at } r=0,\\ u(r)\to 0,\quad T(r)\to T_\infty,\quad v(r)\to 0,\ \text{when } r\to\infty. \end{array}\right\} \tag{9}$$

The thermal characteristics of the tri-hybrid nanofluid are $(\phi_1=\phi_{Ti_6Al_4V},\ \phi_2=\phi_{AA7072},\ \phi_3=\phi_{AA7075})$:

Viscosity

$$\frac{\mu_{\text{Thnf}}}{\mu_f}=\frac{1}{(1-\phi_{Ti_6Al_4V})^{2.5}(1-\phi_{AA7072})^{2.5}(1-\phi_{AA7075})^{2.5}},$$

Table 1 Numerical values of thermophysical characteristics of base fluid and NPs $/\phi_1=\phi_{AA7075},\ \phi_2=\phi_{Ti_6Al_4V}/$ [20, 43, 44]

Properties	ρ/kg m^{-3}	C_p/J kg^{-1}K^{-1}	k/kg ms^{-3}K^{-1}	σ/Ωm^{-1}
$H_2O + C_2H_6O_2$	1063.8	3630	0.387	9.75×10^{-4}
Ti_6Al_4V	4420	0.56	7.2	5.8×10^{5}
AA7072	2720	893	222	34.83×10^{6}
AA7075	2810	960	173	26.77×10^{6}

Density

$$\frac{\rho_{\mathrm{Thnf}}}{\rho_{\mathrm{f}}}=\left(1-\phi_{\mathrm{Ti_6Al_4V}}\right)\left[\left(1-\phi_{\mathrm{Ti_6Al_4V}}\right)\left\{\left(1-\phi_{\mathrm{AA7072}}\right)+\phi_{\mathrm{AA7075}}\frac{\rho_{\mathrm{AA7072}}}{\rho_{\mathrm{f}}}\right\}+\phi_{\mathrm{Ti_6Al_4V}}\frac{\rho_{\mathrm{Ti_6Al_4V}}}{\rho_{\mathrm{f}}}\right]+\phi_{\mathrm{AA7075}}\frac{\rho_{\mathrm{AA7075}}}{\rho_{\mathrm{f}}},$$

$$\left.F'^2=\frac{(K+\eta)}{A_1}P',\right\} \tag{11}$$

$$\left.\begin{aligned}&\tfrac{K}{(\eta+K)}\left(\tfrac{2P}{A_1}\right)=\tfrac{1}{A_1A_2}\left(F'''\tfrac{1}{(K+\eta)}\left(F'-F''\right)\right)+\tfrac{K}{(K+\eta)}\left(F\left(F''+\tfrac{F'}{(K+\eta)}\right)-F'^2\right)\\&-\mathbf{C}F'-\tfrac{A_3A_{31}}{A_1}\mathrm{M}F'-\tfrac{1}{\alpha A_1A_2}\tfrac{\left(1+d_2e^{-\eta}\right)}{\left(1+d_1e^{-\eta}\right)}F'-\beta\tfrac{\left(1+d_2e^{-\eta}\right)^2}{\left(1+d_1e^{-\eta}\right)^{\frac{1}{2}}}F'^2-\mathbf{C}\tfrac{\eta}{2}F''.\end{aligned}\right\} \tag{12}$$

Specific heat

$$\frac{(\rho cp)_{\mathrm{Thnf}}}{(\rho cp)_{\mathrm{f}}}=\phi_{AA7075}\frac{(\rho cp)_{\mathrm{AA7075}}}{(\rho cp)_{\mathrm{f}}}+\left(1-\phi_{\mathrm{AA7075}}\right)\left[\left(1-\phi_{\mathrm{Ti_6Al_4V}}\right)\left\{\left(1-\phi_{\mathrm{AA7072}}\right)+\phi_{\mathrm{AA7072}}\frac{(\rho cp)_{\mathrm{AA7072}}}{(\rho cp)_{\mathrm{f}}}\right\}+\phi_{\mathrm{Ti_6Al_4V}}\frac{(\rho cp)_{\mathrm{Ti_6Al_4V}}}{(\rho cp)_f}\right]$$

Thermal conduction

$$\left.\begin{aligned}\frac{k_{\mathrm{Thnf}}}{k_{\mathrm{hnf}}}&=\left(\frac{k_{\mathrm{AA7072}}+2k_{\mathrm{hnf}}-2\phi_{\mathrm{AA7072}}\left(k_{\mathrm{hnf}}-k_{\mathrm{AA7072}}\right)}{k_{\mathrm{AA7072}}+2k_{\mathrm{hnf}}+\phi_{\mathrm{AA7072}}\left(k_{\mathrm{hnf}}-k_{\mathrm{AA7072}}\right)}\right),\\\frac{k_{\mathrm{hnf}}}{k_{\mathrm{nf}}}&=\left(\frac{k_{\mathrm{Ti_6Al_4V}}+2k_{\mathrm{nf}}-2\phi_{\mathrm{Ti_6Al_4V}}\left(k_{\mathrm{nf}}-k_{\mathrm{Ti_6Al_4V}}\right)}{k_{\mathrm{Ti_6Al_4V}}+2k_{\mathrm{nf}}+\phi_{\mathrm{Ti_6Al_4V}}\left(k_{\mathrm{nf}}-k_{\mathrm{Ti_6Al_4V}}\right)}\right),\\\frac{k_{\mathrm{nf}}}{k_{\mathrm{f}}}&=\left(\frac{k_{\mathrm{AA7075}}+2k_{\mathrm{f}}-2\phi_{\mathrm{AA7075}}\left(k_{\mathrm{f}}-k_{\mathrm{AA7075}}\right)}{k_{\mathrm{AA7075}}+2k_{\mathrm{f}}+\phi_{\mathrm{AA7075}}\left(k_{\mathrm{f}}-k_{\mathrm{AA7075}}\right)}\right),\end{aligned}\right\}$$

Electrical conductivity

$$\begin{aligned}\frac{\sigma_{\mathrm{Thnf}}}{\sigma_{\mathrm{hnf}}}&=\left[1+\frac{3\left(\frac{\sigma_{\mathrm{AA7072}}}{\sigma_{\mathrm{hnf}}}-1\right)\phi_{\mathrm{AA7072}}}{\left(\frac{\sigma_{\mathrm{AA7072}}}{\sigma_{\mathrm{hnf}}}+2\right)-\left(\frac{\sigma_{\mathrm{AA7072}}}{\sigma_{\mathrm{hnf}}}-1\right)\phi_{\mathrm{AA7072}}}\right],\\\frac{\sigma_{\mathrm{hnf}}}{\sigma_{\mathrm{nf}}}&=\left[1+\frac{3\left(\frac{\sigma_{\mathrm{Ti_6Al_4V}}}{\sigma_{\mathrm{nf}}}-1\right)\phi_{\mathrm{Ti_6Al_4V}}}{\left(\frac{\sigma_{\mathrm{Ti_6Al_4V}}}{\sigma_{\mathrm{nf}}}+2\right)-\left(\frac{\sigma_{Ti_6Al_4V}}{\sigma_{\mathrm{nf}}}-1\right)\phi_{\mathrm{Ti_6Al_4V}}}\right],\\\frac{\sigma_{\mathrm{nf}}}{\sigma_{\mathrm{f}}}&=\left[1+\frac{3\left(\frac{\sigma_{\mathrm{AA7075}}}{\sigma_{\mathrm{f}}}-1\right)\phi_{\mathrm{AA7075}}}{\left(\frac{\sigma_{\mathrm{AA7075}}}{\sigma_{\mathrm{f}}}+2\right)-\left(\frac{\sigma_{\mathrm{AA7075}}}{\sigma_{\mathrm{f}}}-1\right)\phi_{\mathrm{AA7075}}}\right]\end{aligned}$$

Considering the variables

$$\left.\begin{aligned}&u=\frac{bs}{(1-\alpha^*t)}F'(\eta),\quad p=\frac{\rho_{\mathrm{f}}(bs)^2}{(1-\alpha^*t)^2}P(\eta),\\&v=-\left(\frac{R}{R+r}\right)\left(\frac{b\nu_{\mathrm{f}}}{1-\alpha^*t}\right)^{\frac{1}{2}}F(\eta),\\&T=T_\infty+(T_w-T_\infty)\theta(\eta),\quad\eta=\sqrt{\frac{u_{\mathrm{w}}}{\nu_{\mathrm{f}}s(1-\alpha^*t)}}r.\end{aligned}\right\} \tag{10}$$

Using Eq. (10), Eq. (3) is satisfied, whereas Eqs. (4)–(6) are converted into:

Putting Eq. (12) into Eq. (11) we have

$$\left.\begin{aligned}&F''''+2\tfrac{F'''}{(\eta+K)}+A_1A_2\left[F\left(F'''+\tfrac{F''}{(K+\eta)}\right)-\left(F''-\tfrac{F'}{(\eta+K)}\left(F'-\tfrac{F}{(\eta+K)}\right)\right)\right]\left(\tfrac{K}{K+\eta}\right)+\tfrac{F'}{(\eta+K)^3}\\&-A_2A_3A_{31}A_{32}\left(\mathrm{M}F''+\tfrac{1}{(K+\eta)}\mathrm{M}F'\right)-\tfrac{A_1A_2\mathbf{C}}{2(K+\eta)}\left(2F'+(K+\eta)\left(3F''+\eta F'''\right)+\eta F''\right)\\&+\tfrac{KF''}{\alpha(K+\eta)^2}\left(e^{-\eta}d_2-F'\left(\tfrac{\left(1+d_2e^{-\eta}\right)}{\left(1+d_1e^{-\eta}\right)^2}e^{-\eta}d_1\right)\left(\tfrac{1+d_2e^{-\eta}}{1+d_1e^{-\eta}}\right)\right)-\tfrac{F''}{(\eta+K)^3}\\&-\tfrac{\beta K}{(K+\eta)^2}\left(2F'F''\left(\tfrac{\left(1+d_2e^{-\eta}\right)^2}{\left(1+d_1e^{-\eta}\right)^{\frac{1}{2}}}\right)+\left(\tfrac{\left(1+d_2e^{-\eta}\right)^2}{2\left(1+d_1e^{-\eta}\right)^{\frac{3}{2}}}d_1e^{-\eta}-2d_2e^{-\eta}\left(1+d_2e^{-\eta}\right)^2\right)F'^2\right)=0,\end{aligned}\right\} \tag{13}$$

$$\left.\begin{aligned}&\theta''+\tfrac{A_5\mathrm{Pr}K}{A_4\times A_{41}\times A_{42}+\mathrm{Ra}(\eta+K)}F\theta'+\tfrac{A_3\times A_{31}\times A_{32}}{A_4\times A_{41}\times A_{42}+\mathrm{Ra}}\mathrm{BrM}F'^2+\tfrac{\mathrm{Pr}S}{A_4\times A_{41}\times A_{42}+\mathrm{Ra}}\theta\\&+\tfrac{\theta'}{\eta+K}+\tfrac{1}{A_4\times A_{41}\times A_{42}+\mathrm{Ra}}\left(\mathrm{Ec}\left(\left(F''+\tfrac{1}{\eta+K}F'\right)^2\right)\right)+\tfrac{\mathrm{Br}}{A_2A_5\alpha\mathrm{Re_s}}\left(\tfrac{1+d_2e^{-\eta}}{1+d_1e^{\eta}}F'^2\right)\\&+\mathrm{Qe}(e^{-n\eta})\theta+\tfrac{A_1\beta}{A_5}\tfrac{\left(1+d_2e^{-\eta}\right)^2}{\left(1+d_1e^{-\eta}\right)^{\frac{1}{2}}}F'^3-\tfrac{\mathbf{C}}{2}\eta(\eta+K)^3\theta'\\&+\beta_1\left(\begin{aligned}&+K(\eta+K)^2\left(\frac{1}{2}f'\theta'+f\theta''\right)\eta\mathbf{C}-\frac{3}{4}\mathbf{C}^2\eta(\eta+K)^3\theta'-\frac{1}{4}\mathbf{C}^2\eta^2(\eta+K)^3\theta''\\&+\frac{3K}{2}\mathbf{C}(\eta+K)^2f\theta'-K^2(\eta+K)f^2\theta''-K^2\left((\eta+K)ff'-f^2\right)\theta'\end{aligned}\right)=0,\end{aligned}\right\} \tag{14}$$

The following are transformed boundary conditions:

$$\left.\begin{aligned}&\text{when}\quad\eta=0,\quad F=0,\quad F'=\theta=1,\\&\text{when}\quad\eta\to\infty,\quad F''=\ F'=\theta\to0.\end{aligned}\right\} \tag{15}$$

In above expressions

$$\left.\begin{aligned}&A_1=\frac{\rho_{\mathrm{Thnf}}}{\rho_{\mathrm{f}}},\ A_2=\frac{\mu_{\mathrm{Thnf}}}{\mu_{\mathrm{f}}},\ A_{31}=\frac{\sigma_{\mathrm{Thnf}}}{\sigma_{\mathrm{hnf}}},\ A_{32}=\frac{\sigma_{\mathrm{hnf}}}{\sigma_{\mathrm{nf}}},\ A_3=\frac{\sigma_{\mathrm{nf}}}{\sigma_{\mathrm{f}}},\\&A_{41}=\frac{k_{\mathrm{Thnf}}}{k_{\mathrm{hnf}}},\ A_{42}=\frac{k_{\mathrm{hnf}}}{k_{\mathrm{nf}}},\ A_4=\frac{k_{\mathrm{nf}}}{k_{\mathrm{f}}},\ A_5=\frac{(\rho c_{\mathrm{p}})_{\mathrm{Thnf}}}{(\rho c_{\mathrm{p}})_{\mathrm{f}}}.\end{aligned}\right\} \tag{16}$$

The dimensionless variables are:

Parameters	Symbols	Expression
Magnetic factor		$M=\frac{\sigma B_0^2}{b\rho_{\mathrm{f}}}$
Radiation parameter	Ra	$\mathrm{Ra}=\frac{16\sigma^*T_\infty^3}{3kk^*}$

Parameters	Symbols	Expression
Eckert number	Ec	$\mathrm{Ec}=\frac{u_w^2}{(T_w-T_\infty)(C_p)_f}$
Permeability term	α	$\alpha=\frac{k_\infty}{\varepsilon_\infty}\frac{\rho_f u_w(1-\alpha^* t)}{\mu_f}$
Unsteadiness parameter	$\mathbf{C}$	$\mathbf{C}=\frac{\alpha^*}{b}$
Non-uniform inertia factor	β	$\beta=\frac{1}{k_\infty^{1/2}}C_b r\varepsilon_\infty$
Exponential heat source	Qe	$\mathrm{Qe}=\frac{Q}{u_w(C_p)_f}$
Prandtl number	Pr	$\mathrm{Pr}=\frac{(\mu C_p)_f}{k_f}$
Curvature parameter	K	$K=R\sqrt{\frac{b}{\nu(1-\alpha^* t)}}$
Thermal relaxation parameter	β_1	$\beta_1=\frac{b\lambda_E}{(1-\alpha^* t)}$
Brinkman number	Br	$\mathrm{Br}=\frac{\mu_f(bs)^2}{(T_w-T_\infty)k_f}$
Rate of entropy generation	N_{EG}	$N_{EG}=\frac{S_{gen}\nu_f T_\infty}{k_f b(T_w-T_\infty)}$
Temperature ratio parameter	γ_1	$\gamma_1=\frac{T_f-T_\infty}{T_\infty}$

The required skin friction and Nusselt number values are as follows:

$$Cf_s=\frac{1}{\rho_f}\left(\frac{\tau_{rs}}{u_w^2}\right),\quad \mathrm{Nu}_s=\frac{1}{k_f}\left(\frac{sq_w}{(T_w-T_\infty)}\right), \tag{17}$$

In Eq. (17) heat flux q_w and wall shear stress τ_{rs} are given as:

$$\begin{aligned} q_w &= -k_{\mathrm{Thnf}}\left(\frac{\partial T}{\partial r}\right)\left(\frac{16\sigma^* T_\infty^3}{3k_f k^*}\frac{k_f}{k_{\mathrm{Thnf}}}+1\right)\Bigg|_{r=0}, \\ \tau_{rs} &= -\mu_{\mathrm{Thnf}}\left(\frac{u}{r+R}-\frac{\partial u}{\partial r}\right)\Bigg|_{r=0}, \end{aligned} \tag{18}$$

By using Eq. (9), the above equations become:

$$\begin{aligned} (\mathrm{Re}_s)^{\frac{-1}{2}}\mathrm{Nu}_s &= A_{41}A_4\left(1+\frac{\mathrm{Ra}}{A_{41}A_4}\right)\theta'(0), \\ (\mathrm{Re}_s)^{\frac{1}{2}}C_{fs} &= \frac{-1}{A_2}\left(\frac{1}{K}f'(0)-f''(0)\right), \end{aligned} \tag{19}$$

where Reynolds's number $\mathrm{Re}_s=\frac{bs^2}{\nu_f}$.

Entropy optimization

The present problem's entropy development is defined as [34]:

$$\begin{aligned} S_{gen} = {} & \frac{k_{\mathrm{Thnf}}}{T_\infty^2}\left(\frac{\partial T}{\partial r}\right)^2+\frac{k_{\mathrm{Thnf}}}{T_\infty^2}\frac{16\sigma^* T_\infty^3}{3kk^*}\left(\frac{\partial T}{\partial r}\right)^2 \\ & +\frac{\mu_{\mathrm{Thnf}}}{T_\infty}\left(\frac{\partial u}{\partial r}\right)^2+\frac{\sigma_{\mathrm{Thnf}}B_0^2}{T_\infty}u^2 \\ & +\frac{Q^* e}{(\rho C_p)_{\mathrm{Thnf}}}(T-T_\infty)\exp\left(-\left(\frac{u_w}{\nu_f}\right)^{\frac{1}{2}}r\right) \\ & +\frac{\mu_{\mathrm{Thnf}}}{(\rho C_p)_{\mathrm{Thnf}}}\frac{\varepsilon(r)}{k^*(r)}u^2+\frac{\rho_{\mathrm{Thnf}}}{(\rho C_p)_{\mathrm{Thnf}}}\frac{\varepsilon(r)}{(k^*(r))^{\frac{1}{2}}}u^3. \end{aligned} \tag{20}$$

Equation (20) can be modified as follows with the use of Eq. (9):

$$\begin{aligned} N_{EG} = {} & A_4A_{41}\gamma_1\theta'^2+A_4A_{41}\gamma_1\mathrm{Ra}\theta'^2 \\ & +\frac{\mathrm{Br}}{A_2}f''^2+A_3A_{31}\mathrm{BrM}F'^2+\mathrm{Pr}S\theta \\ & +\frac{\mathrm{PrQe}}{A_5}e^{-n\eta}\theta+\frac{\mathrm{Br}}{A_2A_5\alpha\mathrm{Re}_s}\left(\frac{1+d_2e^{-\eta}}{1+d_1e^{\eta}}F'^2\right) \\ & +\frac{A_1\beta}{A_5}\frac{(1+d_2e^{-\eta})^2}{(1+d_1e^{-\eta})^{\frac{1}{2}}}F'^3. \end{aligned} \tag{21}$$

Numerical technique and problem validation

The numerical technique PCM is employed for the solution of the proposed model [11, 45, 46]. Scientific study often experiences challenging nonlinear boundary value problems (BVPs) that are challenging to resolve. Many problems, usually addressed by the Newton–Raphson linearization technique, have numerical convergence that depends on differential topology, initial guesses and relaxation variables. In this work, the alternative approach-known as the parametric continuation method—is emphasized. The methodology is consisting of the following steps:

Step 1: simplifications of ODEs to lowest order

The system of Eqs. (13, 14 and 22) along with Eq. (15), is further reset into the lowest order by selecting the following variables:

$$\begin{aligned} F &= \mathfrak{I}_1, F'=\mathfrak{I}_2,\ F''=\mathfrak{I}_3,\ F'''=\mathfrak{I}_4, \\ \theta &= \mathfrak{I}_5,\ \theta'=\mathfrak{I}_6,\ \ N_{EG}=\mathfrak{I}_7. \end{aligned} \tag{22}$$

By incorporating Eq. (22) in Eqs. (13, 14 and 22), we get:

$$\left.\begin{array}{l}\Im_4' + 2\frac{\Im_4}{(\eta+K)} + A_1A_2\left[\Im_1\left(\Im_4 + \frac{\Im_3}{(K+\eta)}\right) - \left(\Im_3 - \frac{\Im_2}{(\eta+K)}\left(\Im_2 - \frac{\Im_1}{(\eta+K)}\right)\right)\right]\left(\frac{K}{K+\eta}\right)\\ + \frac{\Im_2}{(\eta+K)^3} - A_2A_3A_{31}A_{32}\left(M\Im_3 + \frac{1}{(K+\eta)}M\Im_2\right) - \frac{A_1A_2\mathbf{C}}{2(K+\eta)}\begin{pmatrix}2\Im_2 + (K+\eta)\\ (3\Im_3 + \eta\Im_4) + \eta\Im_3\end{pmatrix}\\ + \frac{K\Im_3}{\alpha(K+\eta)^2}\left(e^{-\eta}d_2 - \Im_2\left(\frac{(1+d_2e^{-\eta})}{(1+d_1e^{-\eta})^2}e^{-\eta}d_1\right)\left(\frac{1+d_2e^{-\eta}}{1+d_1e^{-\eta}}\right)\right) - \frac{\Im_3}{(\eta+K)^3}\\ - \frac{\beta K}{(K+\eta)^2}\left(2\Im_1\Im_3\left(\frac{(1+d_2e^{-\eta})^2}{(1+d_1e^{-\eta})^{\frac{1}{2}}}\right) + \left(\frac{(1+d_2e^{-\eta})^2}{2(1+d_1e^{-\eta})^{\frac{3}{2}}}d_1e^{-\eta} - 2d_2e^{-\eta}(1+d_2e^{-\eta})^2\right)\Im_2^2\right) = 0,\end{array}\right\} \quad (23)$$

$$\left.\begin{array}{l}\Im_6' + \frac{A_5\mathrm{Pr}K}{A_4A_{41}A_{42}+\mathrm{Ra}(\eta+K)}\Im_1\Im_6 + \frac{A_3A_{31}A_{32}}{A_4A_{41}A_{42}+\mathrm{Ra}}\mathrm{Br}M\Im_2^2 + \frac{\mathrm{Pr}S}{A_4A_{41}A_{42}+\mathrm{Ra}}\Im_5\\ \Im_6' + \frac{\Im_5}{\eta+K} + \frac{1}{A_4A_{41}A_{42}+\mathrm{Ra}}\left(\mathrm{Ec}\left(\left(\Im_3 + \frac{1}{\eta+K}\Im_2\right)^2\right)\right) + \frac{\mathrm{Br}}{A_2A_5\alpha\mathrm{Re}_s}\left(\frac{1+d_2e^{-\eta}}{1+d_1e^{\eta}}\Im_3^2\right)\\ +\mathrm{Qe}(e^{-n\eta})\Im_5 + \frac{A_1\beta}{A_5}\frac{(1+d_2e^{-\eta})^2}{(1+d_1e^{-\eta})^{\frac{1}{2}}}\Im_2^3 - \frac{\mathbf{C}}{2}\eta(\eta+K)^3\Im_6\\ +\beta_1\begin{pmatrix}+K(\eta+K)^2\left(\frac{1}{2}\Im_2\theta' + \Im_1\Im_6'\right)\eta\mathbf{C} - \frac{3}{4}\mathbf{C}^2\eta(\eta+K)^3\Im_6 - \frac{1}{4}\mathbf{C}^2\eta^2(\eta+K)^3\Im_6'\\ +\frac{3K}{2}\mathbf{C}(\eta+K)^2\Im_1\Im_6 - K^2(\eta+K)\Im_1^2\Im_6' - K^2((\eta+K)\Im_1\Im_2 - \Im_1^2)\Im_6\end{pmatrix} = 0,\end{array}\right\} \quad (24)$$

The transformed boundary conditions for the first-order fractional differential equations are as:

$$\left.\begin{array}{lll}\Im_1(0) = 0, & \Im_2(0) = 0, & \Im_5(0) = 1,\\ \Im_3(\infty) \to 0, & \Im_2(\infty) \to 0, & \Im_5(\infty) \to 0.\end{array}\right\} \quad (25)$$

Step 2: introducing continuation parameter "*p*"

Step 3: solving the Cauchy problems

By employing the implicit numerical scheme as:

$$\frac{U^{i+1} - U^{i}}{\Delta\eta} = AU^{i+1} \text{ and } \frac{W^{i+1} - W^{i}}{\Delta\eta} = AW^{i+1}. \quad (28)$$

The final iterative form is obtained as:

$$\left.\begin{array}{l}\Im_4' + \left(\frac{2}{(\eta+K)} + A_1A_2\Im_1 - \frac{A_1A_2\mathbf{C}}{2}\eta\right)(\Im_4 - 1)p + A_1A_2\left[-\left(\Im_3 - \frac{\Im_2}{(\eta+K)}\left(\Im_2 - \frac{\Im_1}{(\eta+K)}\right)\right)\right]\\ \left(\frac{K}{K+\eta}\right) - A_2A_3A_{31}A_{32}\left(M\Im_3 + \frac{1}{(K+\eta)}M\Im_2\right) + \frac{\Im_2}{(\eta+K)^3} - \frac{A_1A_2\mathbf{C}}{2(K+\eta)}\begin{pmatrix}2\Im_2 + 3\Im_3\\ (K+\eta) + \eta\Im_3\end{pmatrix}\\ + \frac{K\Im_3}{\alpha(K+\eta)^2}\left(e^{-\eta}d_2 - \Im_2\left(\frac{(1+d_2e^{-\eta})}{(1+d_1e^{-\eta})^2}e^{-\eta}d_1\right)\left(\frac{1+d_2e^{-\eta}}{1+d_1e^{-\eta}}\right)\right) - \frac{\Im_3}{(\eta+K)^3} + A_1A_2K\frac{\Im_1\Im_3}{(K+\eta)^2}\\ - \frac{\beta K}{(K+\eta)^2}\left(2\Im_1\Im_3\left(\frac{(1+d_2e^{-\eta})^2}{(1+d_1e^{-\eta})^{\frac{1}{2}}}\right) + \left(\frac{(1+d_2e^{-\eta})^2}{2(1+d_1e^{-\eta})^{\frac{3}{2}}}d_1e^{-\eta} - 2d_2e^{-\eta}(1+d_2e^{-\eta})^2\right)\Im_2^2\right) = 0,\end{array}\right\} \quad (26)$$

$$\left.\begin{array}{l}\Im_6' + \left(\frac{A_5\mathrm{Pr}K}{A_4A_{41}A_{42}+\mathrm{Ra}(\eta+K)}\Im_1 - \frac{\mathbf{C}}{2}\eta(\eta+K)^3 - \frac{3}{4}\beta_1\mathbf{C}^2\eta(\eta+K)^3 + \frac{3K}{2}\beta_1\mathbf{C}(\eta+K)^2\Im_1\right)\\ (\Im_6 - 1)p + \Im_6' + \frac{\Im_5}{\eta+K} + \frac{1}{A_4A_{41}A_{42}+\mathrm{Ra}}\left(\mathrm{Ec}\left(\left(\Im_3 + \frac{1}{\eta+K}\Im_2\right)^2\right)\right) + \frac{\mathrm{Br}}{A_2A_5\alpha\mathrm{Re}_s}\left(\frac{1+d_2e^{-\eta}}{1+d_1e^{\eta}}\Im_3^2\right)\\ +\mathrm{Qe}(e^{-n\eta})\Im_5 + \frac{A_1\beta}{A_5}\frac{(1+d_2e^{-\eta})^2}{(1+d_1e^{-\eta})^{\frac{1}{2}}}\Im_2^3 + \frac{\mathrm{Pr}S}{A_4A_{41}A_{42}+Ra}\Im_5 + \frac{A_3A_{31}A_{32}}{A_4A_{41}A_{42}+Ra}\mathrm{Br}M\Im_2^2\\ +\beta_1\begin{pmatrix}+K(\eta+K)^2\left(\frac{1}{2}\Im_2\theta' + \Im_1\Im_6'\right)\eta\mathbf{C} - \frac{1}{4}\mathbf{C}^2\eta^2(\eta+K)^3\Im_6'\\ -K^2(\eta+K)\Im_1^2\Im_6' - K^2((\eta+K)\Im_1\Im_2 - \Im_1^2)\Im_6\end{pmatrix} = 0,\end{array}\right\} \quad (27)$$

Table 2 Comparative analysis of current results with the published work

K	Hayat et al. [42]	Hayat et al. [43]	Sajid et al. [47]	Present results
5.0	1.1576	1.1584	0.7576	1.158667
10	1.0735	1.0738	0.8735	1.074142
20	1.0356	1.0339	0.9356	1.034362
30	1.0235	1.0240	0.9569	1.024157
40	1.0176	1.0171	0.9676	1.017410
50	1.0141	1.0147	0.9741	1.014435

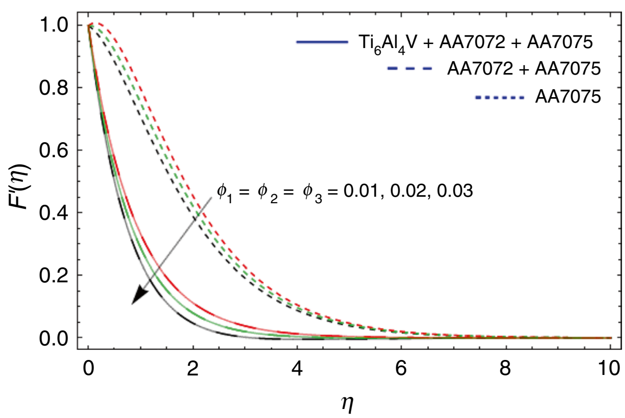

Fig. 2 Impact of volume friction parameters on $F'(\eta)$

$$U^{i+1} = \frac{U^i}{(I - \Delta\eta A)} \quad \text{and} \quad W^{i+1} = \frac{(W^i + \Delta\eta R)}{(I - \Delta\eta A)}. \tag{29}$$

Validation of results

Comparing the present results to previously published work for $m = 1$ and numerous values of K is illustrated

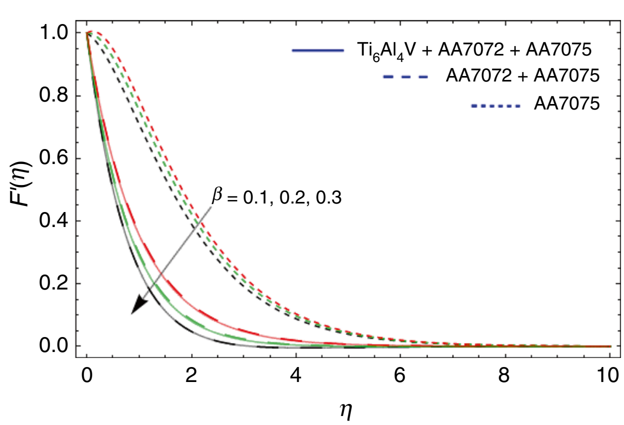

Fig. 3 Impact of inertia coefficient β on $F'(\eta)$

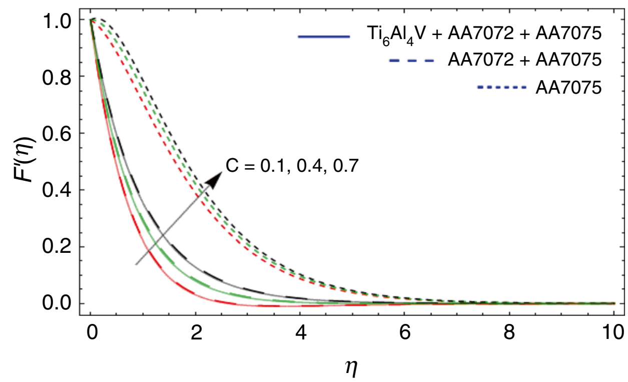

Fig. 4 Impact of unsteadiness parameter **C** on $F'(\eta)$

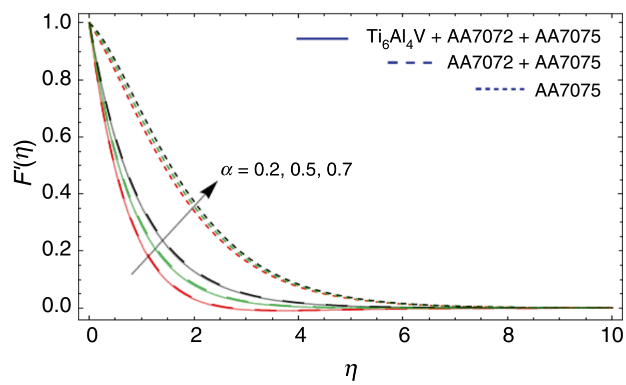

Fig. 5 Impact of permeability parameter on $F'(\eta)$

in Table 2. It can be noticed that the both results show remarkable similarity.

Discussion and graphical results

This section examines the variances in entropy generation, velocity, temperature gradient, and skin friction, concerning various physical features. The entropy formation in

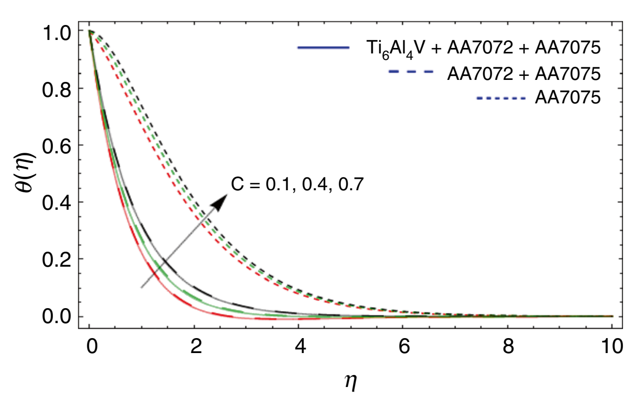

Fig. 6 Impact of unsteadiness parameter **C** on $\theta(\eta)$

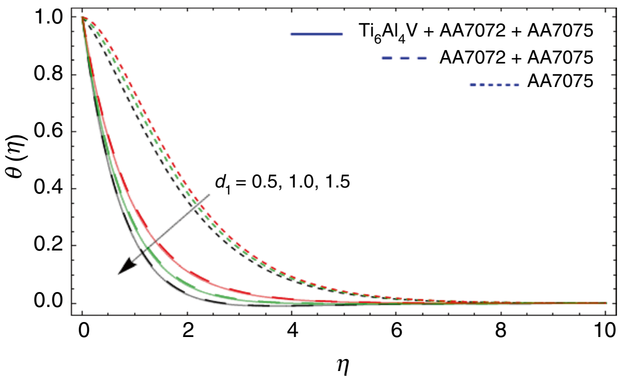

Fig. 7 Impact of variable permeability d_1 on $\theta(\eta)$

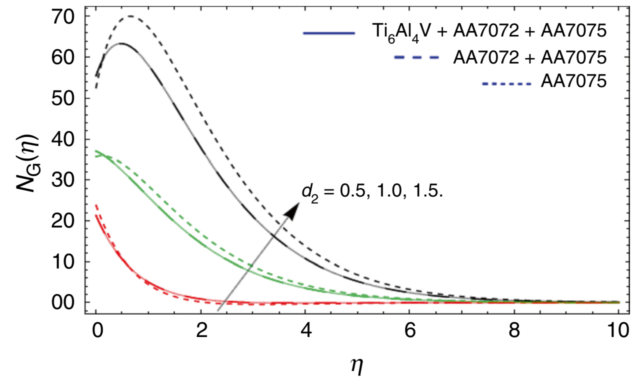

Fig. 10 Impact of variable porosity d_2 versus $N_G(\eta)$

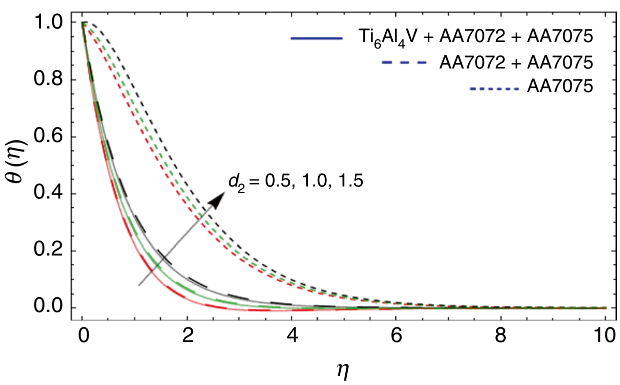

Fig. 8 Impact of variable porosity d_2 on $\theta(\eta)$

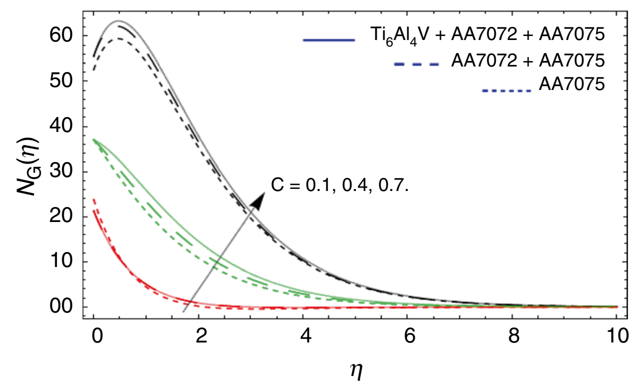

Fig. 11 Impact of unsteadiness parameter **C** versus $N_G(\eta)$

a Thnf flow through a CSS under the influence of exponential heat source/sink is assessed in the current investigation. The results are obtained through PCM. In these illustrations, solid lines represent the Thnf, dashed lines reflect the Hnf, and dot lines indicate the NF. The primary findings are addressed as follows:

Figures 2–5 demonstrate the outcome of volume fraction $(\phi_1,\ \phi_2,\ \phi_3)$ inertia coefficient β, unsteadiness parameter **C**, permeability parameter α on the fluid velocity. The outcome of the volume fraction on the velocity is extensively represented in Fig. 2. As the numbers of NPs rises, the fluid velocity falls due to the intensified fluid resistance. In addition, Fig. 2 demonstrates that the ternary hybrid nanofluid has a greater impact on reducing velocity compared to the binary and conventional nanofluids. Figure 3 depicts the effect of β on velocity. An improved internal force is produced by a higher value of β, which elevates velocity. Figure 4 shows an illustration

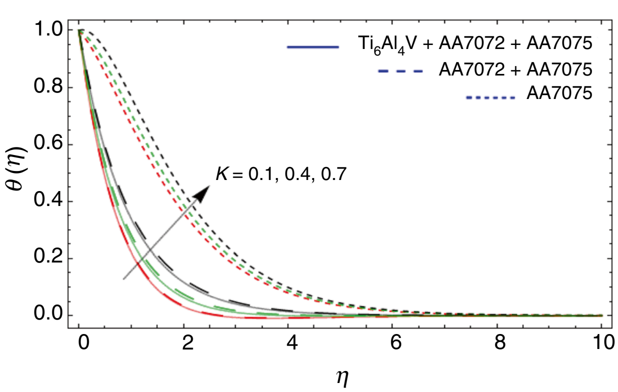

Fig. 9 Impact of curvature parameter K on $\theta(\eta)$

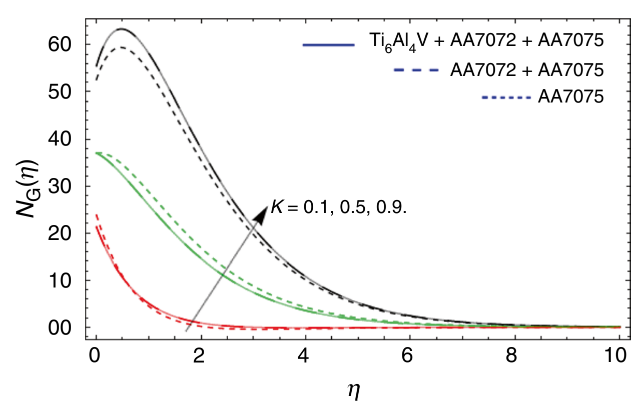

Fig. 12 Impact of curvature parameter K versus $N_G(\eta)$

Table 3 Numerical results for skin friction Cf_s

Parameters				Cf_s	
M	d_1	d_2	α	Hybrid nanofluid	Tri-hybrid nanofluid
0.1	0.5	0.5	0.1	0.4812387	0.8084224
0.3				1.7324865	2.2642776
0.5				1.4242302	2.1871587
0.1	1.0			1.3780276	2.1119820
	1.5			1.4230665	2.1311153
	2.0			1.2178728	2.8281276
	0.5	1.0		1.1416390	2.7517102
		1.5		1.0328342	2.8023123
		2.0		1.2762962	2.2960270
		0.5	0.2	1.2220764	2.8103432
			0.3	1.5148910	2.1612856
			0.4	1.7923092	2.4439433

Table 4 Numerical outputs for Nusselt number Nu_s

Parameters					Nu_s	
Br	d_1	d_2	**C**	Qe	Hybrid nanofluid	Tri-hybrid nanofluid
0.1	0.5	0.5	0.1	0.2	1.710206	2.312538
					1.543827	2.034628
					1.230564	1.732731
0.1					0.632028	1.032138
0.4					0.722078	1.370281
0.7					1.172611	1.319611
1.1	1.0				0.622148	1.141571
	1.5				0.732046	1.401528
	2.0				0.892330	1.731105
	2.5	1.0			0.812052	1.632801
		1.5			0.721145	1.341207
		2.0			0.609830	1.011386
		2.5	0.1		2.247161	2.830412
			0.2		2.014301	2.701212
			0.3		1.880292	2.408911
			0.4	0.2	0.816212	1.450850
				0.5	0.695315	1.189146
				0.8	0.402113	1.083181

of the velocity curve $F'(\eta)$ against the unsteadiness factor **C**. There is a correlation between higher values of the unsteadiness parameter **C** and an increase in velocity $F'(\eta)$. Figure 4 shows that ternary hybrid nanofluid boosted the velocity more than hybrid and nano-fluids. The consequences of permeability parameter α on velocity $F'(\eta)$ are illustrated in Fig. 5. Rising values of α led to a corresponding increase in velocity. Higher permeability coefficient enables fluid to flow more effortlessly, leading to increased velocities and flow rates. As seen in Fig. 5 Thnf exhibits a greater impact on the increase in velocity when compared to both NF and Hnf.

The effects of the unsteadiness parameter **C**, variable permeability d_1, variable porosity d_2, and curvature parameter K on the temperature distribution are illustrated in Figs. 6–9. Figure 6 describes the upshot of $\mathbf{C}$ on the temperature field $\theta(\eta)$. Greater values of the unsteadiness parameter $\mathbf{C}$ result in a more intense temperature field $\theta(\eta)$ and an increased thickness of the thermal layer. As the unsteadiness variable $\mathbf{C}$ increases, there is a decrease in the amount of heat that flows from the surface to the fluid, consequently, the temperature $\theta(\eta)$ falls. Variable permeability and porosity factors effect on temperature $\theta(\eta)$ is seen in Figs. 7 and 8. The ability of a substance or substrate to permit fluids or substances to pass through it is called its variable permeability. An decline in $\theta(\eta)$ is reported for higher values of d_1. Fluids with higher permeability d_1 can move relatively easily which reduce the convective heat transfer. Figure 8 exhibit the behavior of temperature $\theta(\eta)$ against different values of d_2. Lower flow resistance is usually the result of higher number of variable porosity d_2, which increases the number of pores for fluid flow which boosts the flow rate of the fluid and consequently accelerates the heat transfer rates. The influence of the curvature parameter on $\theta(\eta)$ is addressed in Fig. 9.

Figures 10–12 discussed the generation of entropy against variable porosity d_2 unsteadiness parameter $\mathbf{C}$ and curvature parameter K. The influence of variable porosity d_2 is depicted in Fig. 10. A rise in variable porosity d_2 causes an upsurge in entropy production. As a result of the variation in variable porosity, non-uniform flow patterns emerge, or flow instabilities are induced. Additionally, the amount of entropy generation increased. A graphic representation of entropy formation for varying values of $\mathbf{C}$ is shown in Fig. 11. Higher entropy formation is observed with larger values of the unsteadiness parameter. Figure 12 discussed the entropy generation against curvature parameter K. A spike in entropy production is caused by a rise in the curvature parameter. Due to the radial boundary's configuration, Fig. 12 revealed that an increase in the radius's curvature parameter will result in a decrease in the entropy profile. Furthermore, it is noted that ternary hybrid nanofluid improves entropy optimization noticeably more than hybrid and nano-fluid.

Table 3 demonstrates the numerical outcomes of $\sqrt{\mathrm{Re}}\mathrm{Cf}_r$. As the variable permeability, and magnetic parameter M increases, the coefficient of skin friction diminishes, while increase in permeability parameter α, variable unsteadiness parameter $\mathbf{C}$ and variable porosity improved the skin friction of the fluid. Table 4 illustrates the variation of the Nu_r as a function of the various physical parameters. Nu_r boosts as there is more heat owing to variable permeability d_1, and Brinkman number and decline with increase in inertia coefficient β_1, variable porosity, unsteadiness parameter $\mathbf{C}$ and Exponential heat source.

Conclusions

Optimizing the entropy production of magnetized Darcy–Forchheimer ternary hybrid flow of nanoliquid on a porous curved stretched surface is the focus of this study. In order to synthesize the modified hybrid nanofluid, Ti_6Al_4V, AA7072 and AA7075-NPs are added to water and ethylene glycol (50% + 50%). The need to speed up heat transfer for industrial and engineering applications inspired the present study. The novel findings are as follows:

- In comparison with NF and Hnf, the Thnf exhibits dominant behavior.
- Combining ethylene glycol and water improves efficiency of heat transfer.
- Heat transmission in base fluid is positively influenced by the addition of Ti_6Al_4V, AA7072 and AA7075-NPs.
- The inertia coefficient has a negative effect on the velocity distribution; while, larger values of the permeability parameter have a positive effect on the distribution of velocity.
- Strengthening curvature parameter and fluctuating porosity increased temperature.
- Improvements in the unsteadiness parameter and varying porosity lead to increases in Entropy production.
- Skin friction declines as the variable porosity increases.
- Higher Br values result in a higher Nusselt number; while, low Ra and Qe. values result in a smaller Nusselt number.

Acknowledgements The authors extend their appreciation to the Deanship of Research and Graduate Studies at King Khalid University for funding this work through Large Research Project under grant number RGP2/524/45

Data availability All relevant data are included in the article.

References

1. Ullah B, Fadhl BM, Makhdoum BM, Nisar KS, Wahab HA, Khan U. Heat transfer analysis in Darcy Forchheimer flow of hybrid nanofluid for multiple shape effects over a curved stretching surface. Case Stud Therm Eng. 2022;40: 102538.
2. Saeed Khan GT, Khan I, Gul T, Bilal M. Mixed convection and thermally radiative hybrid nanofluid flow over a curved surface. Adv Mech Eng. 2022;14(3):16878132221082848.
3. Abbas N, Rehman KU, Shatanawi W, Malik M. Numerical study of heat transfer in hybrid nanofluid flow over permeable nonlinear stretching curved surface with thermal slip. Int Commun Heat Mass Transf. 2022;135: 106107.
4. Raza R, Mabood F, Naz R, Abdelsalam SI. Thermal transport of radiative Williamson fluid over stretchable curved surface. Therm Sci and Eng Prog. 2021;23: 100887.

5. Ahmed K, Akbar T, Muhammad T. Physical aspects of homogeneous-heterogeneous reactions on MHD Williamson fluid flow across a nonlinear stretching curved surface together with convective boundary conditions. Math Probl Eng. 2021;2021:1–13.
6. Xiong P-Y, Javid K, Raza M, Khan SU, Khan MI, Chu Y-M. MHD flow study of viscous fluid through a complex wavy curved surface due to bio-mimetic propulsion under porosity and second-order slip effects. Commun Theor Phys. 2021;73(8): 085001.
7. Ali B, Jubair S. Rheological properties of Darcy-Forchheimer hybrid nanofluid flow with thermal emission and heat source over a curved slippery surface. Pramana. 2023;97(3):127.
8. Hayat AU, Ullah I, Khan H, Alam MM, Hassan AM, Khan H. Numerical analysis of radiative hybrid nanomaterials flow across a permeable curved surface with inertial and Joule heating characteristics. Heliyon. 2023. https://doi.org/10.1016/j.heliyon.2023.e21452.
9. Imran M, Naveed M, Abbas Z. Dynamics of Soret and Dufour effects on oscillatory flow of couple stress fluid due to stretchable curved surface. Adv Mech Eng. 2023;15(2):16878132231156742.
10. Ul-Haq S, Ashraf MB. Entropy analysis in MHD convective flow of Carreau fluid over a curved stretching surface with soret and dufour effects. Numer Heat Transf, Part A: Appl. 2024;85(11):1780–99.
11. Murtaza S, Kumam P, Bilal M, Sutthibutpong T, Rujisamphan N, Ahmad Z. Parametric simulation of hybrid nanofluid flow consisting of cobalt ferrite nanoparticles with second-order slip and variable viscosity over an extending surface. Nanotechnol Rev. 2023;12(1):20220533.
12. Ali B, Liu S, Liu H. An application of artificial neural network toward the mathematical modeling of mhd tangent hyperbolic nanofluid across a vertical stretching surface. J Porous Med. 2024. https://doi.org/10.1615/JPorMedia.2024051939.
13. Alrabaiah H, Iftikhar S, Saeed A, Bilal M, Eldin SM, Galal AM. Numerical calculation of Darcy Forchheimer radiative hybrid nanofluid flow across a curved slippery surface. S Afr J Chem Eng. 2023;45:172–81.
14. Ali B, Jubair S, Aluraikan A, Abd El-Rahman M, Eldin SM, Khalifa H-W. Numerical investigation of heat source induced thermal slip effect on trihybrid nanofluid flow over a stretching surface. Res Eng. 2023;20:101536.
15. Choi SU, Eastman JA. Enhancing thermal conductivity of fluids with nanoparticles: Argonne National Lab.(ANL), Argonne, IL (United States)1995.
16. Buongiorno J. Convective transport in nanofluids. J Heat Transf. 2006;128(3):240–50.
17. Makkar V, Dang K, Sharma N, Yadav S. Numerical investigation of MHD convective free stream nanofluid flow influenced by radiation and chemical reaction over stretching cylinder. Heat Transf. 2023;52(3):2328–47.
18. Ullah I, Hayat T, Alsaedi A, Asghar S. Dissipative flow of hybrid nanoliquid (H2O-aluminum alloy nanoparticles) with thermal radiation. Phys Scr. 2019;94(12): 125708.
19. Hanif H, Jamshed W, Eid MR, Ibrahim RW, Shafie S, Raezah AA, et al. Numerical Crank-Nicolson methodology analysis for hybridity aluminium alloy nanofluid flowing based-water via stretchable horizontal plate with thermal resistive effect. Case Stud Therm Eng. 2023;42: 102707.
20. Tlili I, Nabwey HA, Ashwinkumar G, Sandeep N. 3-D magnetohydrodynamic AA7072-AA7075/methanol hybrid nanofluid flow above an uneven thickness surface with slip effect. Sci Rep. 2020;10(1):1–13.
21. Archana M, Kumar KG, Prakasha D, Vasanth K, Khan MI. Improvement for heat transfer applications through a ternary alloy on flow over a melted sheet. Int J Thermofluids. 2023;20: 100505.
22. Manjunatha S, Puneeth V, Baby AK, Vishalakshi C. Examination of thermal and velocity slip effects on the flow of blood suspended with aluminum alloys over a bi-directional stretching sheet: the ternary nanofluid model. Waves Random Complex Med. 2022. https://doi.org/10.1080/17455030.2022.2056260.
23. Li S, Faizan M, Ali F, Ramasekhar G, Muhammad T, Khalifa H-W, et al. Modelling and analysis of heat transfer in MHD stagnation point flow of Maxwell nanofluid over a porous rotating disk. Alex Eng J. 2024;91:237–48.
24. Ahmad Z, Crisci S, Murtaza S, Toraldo G. Numerical insights of fractal–fractional modeling of magnetohydrodynamic Casson hybrid nanofluid with heat transfer enhancement. Math Methods Appl Sci. 2024. https://doi.org/10.1002/mma.10059.
25. Adnan AW, Said NM, Mishra NK, Mahmood Z, Bilal M. Significance of coupled effects of resistive heating and perpendicular magnetic field on heat transfer process of mixed convective flow of ternary nanofluid. J Therm Anal Calorim. 2024;149(2):879–92.
26. Bilal M, Ali A, Mahmoud SR, Tag-Eldin E, Balubaid M. Fractional analysis of unsteady radiative brinkman-type nanofluid flow comprised of CoFe2O3 nanoparticles across a vertical plate. J Therm Anal Calorim. 2023;148(24):13869–82.
27. Bilal M, Ahmed AE-S, El-Nabulsi RA, Ahammad NA, Alharbi KAM, Elkotb MA, et al. Numerical analysis of an unsteady, electroviscous, ternary hybrid nanofluid flow with chemical reaction and activation energy across parallel plates. Micromachines. 2022;13(6):874.
28. Elattar S, Helmi MM, Elkotb MA, El-Shorbagy M, Abdelrahman A, Bilal M, et al. Computational assessment of hybrid nanofluid flow with the influence of hall current and chemical reaction over a slender stretching surface. Alex Eng J. 2022;61(12):10319–31.
29. Ali B, Jubair S. Motile microorganism-based ternary nanofluid flow with the significance of slip condition and magnetic effect over a Riga plate. J Therm Anal Calorim. 2023;148(20):11203–13.
30. ur Rahman M, Haq F, Ijaz Khan M, Awwad FA, Ismail EA. Numerical assessment of irreversibility in radiated sutterby nanofluid flow with activation energy and Darcy Forchheimer. Sci Rep. 2023;13(1):18982.
31. Khan MI, Alzahrani F. Nonlinear dissipative slip flow of Jeffrey nanomaterial towards a curved surface with entropy generation and activation energy. Math Comput Simul. 2021;185:47–61.
32. Naveed M. Analysis of entropy generation of a chemically reactive nanofluid by using Joule heating effect for the Blasius flow on a curved surface. Chem Phys Lett. 2023;826: 140682.
33. Ibrahim W, Gizewu T. Analysis of entropy generation of bio-convective on curved stretching surface with gyrotactic microorganisms and third order slip flow. Int J Thermofluids. 2023;17: 100277.
34. Hayat AU, Ullah I, Khan H, Weera W, Galal AM. Numerical simulation of entropy optimization in radiative hybrid nanofluid flow in a variable features Darcy-Forchheimer curved surface. Symmetry. 2022;14(10):2057.
35. Alsallami SA, Zahir H, Muhammad T, Hayat AU, Khan MR, Ali A. Numerical simulation of Marangoni Maxwell nanofluid flow with Arrhenius activation energy and entropy anatomization over a rotating disk. Waves Random Complex Med. 2022. https://doi.org/10.1080/17455030.2022.2045385.
36. Murtaza S, Kumam P, Sutthibutpong T, Suttiarporn P, Srisurat T, Ahmad Z. Fractal-fractional analysis and numerical simulation for the heat transfer of ZnO+ Al2O3+ TiO2/DW based ternary hybrid nanofluid. ZAMM-J Appl Math Mech/Zeitschrift für Angewandte Mathematik und Mechanik. 2023;104: e202300459.
37. Sakkaravarthi K, Bala Anki Reddy P. Entropy generation on MHD flow of Williamson hybrid nanofluid over a permeable curved stretching/shrinking sheet with various radiations. Numer Heat Transf, Part B: Fundam. 2024;85(3):231–57.

38. Alqahtani AM, Bilal M, Riaz MB, Chammam W, Shafi J, Rahman M, et al. Forced convective tangent hyperbolic nanofluid flow subject to heat source/sink and Lorentz force over a permeable wedge: numerical exploration. Nanotechnol Rev. 2024;13(1):20240014.
39. Ali B, Liu S, Jubair S, Khalifa HAE-W, El Rahman MA. Exploring the impact of Hall and ion slip effects on mixed convective flow of Casson fluid Model: A stochastic investigation through non-Fourier double diffusion theories using ANNs techniques. Therm Sci Eng Prog. 2023;46: 102237.
40. Rafique K, Mahmood Z, Adnan KU, Muhammad T, El Rahman MA, et al. Numerical investigation of entropy generation of Joule heating in non-axisymmetric flow of hybrid nanofluid towards stretching surface. J Comput Des Eng. 2024;11(2):146–60.
41. Khan I, Chinyoka T, Ismail EA, Awwad FA, Ahmad Z. MHD flow of third-grade fluid through a vertical micro-channel filled with porous media using semi implicit finite difference method. Alex Eng J. 2024;86:513–24.
42. Hayat T, Haider F, Muhammad T, Alsaedi A. Darcy-Forchheimer flow due to a curved stretching surface with Cattaneo-Christov double diffusion: a numerical study. Res Phys. 2017;7:2663–70.
43. Abbas AW, Alqahtani AM, Mahmood Z, Ould Beinane SA, Bilal M. Numerical heat featuring in radiative convective ternary nanofluid under induced magnetic field and heat generating source. Int J Mod Phys B. 2024. https://doi.org/10.1142/S0217979225500444.
44. Bani-Fwaz MZ, Fayyaz S, Mishra NK, Mahmood Z, Khan SU, Bilal M. Investigation of unsteady nanofluid over half infinite domain under the action of parametric effects and EPNM. J Therm Anal Calorim. 2024. https://doi.org/10.1007/s10973-024-13121-8.
45. Shuaib M, Shah RA, Durrani I, Bilal M. Electrokinetic viscous rotating disk flow of Poisson-Nernst-Planck equation for ion transport. J Mol Liq. 2020;313: 113412.
46. Raizah Z, Saeed A, Bilal M, Galal AM, Bonyah E. Parametric simulation of stagnation point flow of motile microorganism hybrid nanofluid across a circular cylinder with sinusoidal radius. Open Phys. 2023;21(1):20220205.
47. Sajid M, Ali N, Javed T, Abbas Z. Stretching a curved surface in a viscous fluid. Chin Phys Lett. 2010;27(2): 024703.